Materials & Design 234 (2023) 112296

Contents lists available at ScienceDirect

Materials & Design

journal homepage: www.elsevier.com/locate/matdes

Estimation of directional single crystal elastic properties from nano-indentation by correlation with EBSD and first-principle calculations

Mattis Seehaus [a,1,*], Sang-Hyeok Lee [a,1], Tobias Stollenwerk [a], Jeffrey M. Wheeler [b,c], Sandra Korte-Kerzel [a]

[a] Institut für Metallkunde und Materialphysik, RWTH Aachen University, 52074 Aachen, Germany
[b] Laboratory of Metal Physics and Technology, Department of Materials, ETH Zürich, 8093 Zurich, Switzerland
[c] FemtoTools AG, Furtbachstrasse 4, CH-8107 Buchs/ZH, Switzerland

ARTICLE INFO

Keywords:
Nano-indentation
Stiffness tensor
Least-squares optimisation
Austenitic steel
Meteorite
DFT
EBSD
EDS

ABSTRACT

In this study, a two-step optimisation process for the estimation of the single crystal stiffness tensor from the indentation modulus is presented. This was accomplished by using a 2-dimensional data correlation method for nano-indentation, EBSD and ab initio data, as well as EDS for phase separation in a multi-phase material. Here, a single-phase Fe-24Ni-0.4C austenitic steel and a two-phase Fe-9.5Ni-0.5Co Seymchan meteorite were used as example materials.

In a first step, the combination of high-speed nano-indentation mapping data with elemental and orientation distribution maps allowed the estimation of indentation moduli along specific crystal surface planes normal directions, (001), (011) and (111) using a least squares optimisation based on starting values from DFT or experimentally determined stiffness tensors. A second global optimisation step to estimate the single crystal stiffness tensor using pre-solved solution parameters of the Vlassak-Nix equations yielded reasonable correspondence between the experimentally determined stiffness tensors from correlative nano-indentation data and other methods. The presented method demonstrates generally the possibility to derive directionally sensitive elastic properties from high-speed nano-indentation for cubic materials statistically.

1. Introduction

The development of new materials, whether for structural or functional applications, increasingly focuses on smaller scales and includes the representation of all individual components making up advanced, multi-phase microstructures. For this, many conventional methods of material characterisation have been extended to provide data at small scales and efforts to achieve characterisation across large areas while combining different types of information [1,2]. For example, research methods such as orientation imaging and chemical analysis inside the scanning electron microscope (SEM), first-principle and atomistic simulations as well as nano-indentation have provided new insights and enable multi-scale approaches to measure, predict and interrelate local properties [3–7].

The nano-indentation technique has become particularly effective in evaluating the mechanical properties of materials in combination with a variety of other methods, such as finite element simulations [8,9] or first-principle calculations [10] to correlate plastic and elastic properties or energy dispersive spectroscopy (EDS) to achieve phase mapping [11,12]. Efforts were also made to correlate not only with a single technique, but with two or more methods. Using the example of a $Mn_{15}Si_{26}$ compound, combined nano-indentation, electron backscatter diffraction (EBSD) and elastic moduli calculated from first principles were used to analyse the elastic properties across several grains [13]. Furthermore, correlative nano-indentations were conducted to elucidate the orientation-dependent elastic modulus in conjunction with EBSD analysis. Commercially pure titanium was indented with different indenter geometries to obtain the reduced modulus represented in an inverse pole figure (IPF) [14]. Similarly, EBSD and nano-indentation measurements for lithium metal have been correlated and also used to extract directional variations of the indentation modulus visualised by plotting in an IPF [15].

Although high-speed nano-indentation (NIT) is steadily gaining popularity, correlative research using NIT is still limited due to a lack of

* Corresponding author.
E-mail address: seehaus@imm.rwth-aachen.de (M. Seehaus).
[1] These authors contributed equally to this work.

https://doi.org/10.1016/j.matdes.2023.112296
Received 30 June 2023; Received in revised form 30 August 2023; Accepted 30 August 2023
Available online 9 September 2023
0264-1275/© 2023 The Author(s). Published by Elsevier Ltd. This is an open access article under the CC BY-NC-ND license (http://creativecommons.org/licenses/by-nc-nd/4.0/).

easily accessible tools and the challenges in error-correction. Especially the correction of spatial sampling errors can be a tedious process for data from independent measurements for correlative analysis, as distortions in property maps, EBSD and a NIT grid, are considered independently. Even though the measurement of the EBSD data itself is convenient, the associated distortions caused by thermal drift, electromagnetic field and sample tilt often lead to spatial discrepancies between NIT- and EBSD-results [16]. In a previous study, the XPCorrelate library was developed based on the MATLAB® environment to solve some of these correlation and correction issues [17].

Once spatial correlation is achieved, the next objectives often involve making predictions or comparisons of the identified correlations with theory.

The main objective of this study is therefore to develop a versatile and extendable open-source Python-based point-to-point correlation library for orientation/phase analysis from EBSD/EDS with nano-indentation data. Ultimately, the goal is to enable the estimation of a directional indentation modulus for specific crystal orientations and the single-crystal stiffness tensor from further analysis.

Therefore, the analysis will expand beyond the visualisation of directional elastic properties in IPFs to quantitative estimates of directional and single crystal elastic properties. Nano-indentation is very well suited to acquire the sub-grain mechanical data required for this. However, it is limited in resolving orientation-dependent properties, as the three-dimensional stress field includes contributions from many crystallographic directions. On the other hand, the stiffness tensor is perhaps the mechanical property with the largest theoretical data available or most straightforwardly obtainable from ab initio predictions. Therefore, the main focus is not only to achieve spatial correlation but also use the correlative orientation and indentation modulus data to extract the experimental stiffness tensor from large high-speed NIT data sets and compare it with first principles calculations.

There have been several attempts to estimate the stiffness tensor of a single crystal based on indentation tests [13,15,18]. Most of these approaches are based on the Vlassak-Nix model [19] (V-N), but a major disadvantage of the complex V-N model is that the evaluation of the equation is computationally intensive. One way to overcome this complex evaluation of the constituting equations of the V-N model is using a pre-compiled solution for cubic materials. In this case, the precise evaluation of the indentation modulus for specific low-index planes is required, which is not always convenient.

In order to work around this limitation, a two-step optimisation process is proposed in this study. In the first optimisation step, the indentation stiffness tensor is constructed to determine the indentation moduli along specific (0 0 1), (0 1 1), and (1 1 1) planes normal directions and in a second optimisation step, the elastic constants C_{11}, C_{12} and C_{44} are predicted by applying sets of correction factors proposed by Vlassak and Nix [19].

The developed library presented in this paper enables a self-documenting correlation procedure between experimental and simulative methods, e.g., EBSD, high-speed NIT, SEM, optical microscopy, first-principle calculations and other scientific techniques, using a single phase Fe-24Ni-0.4C austenitic steel and a two-phase Fe-9.5Ni-0.5Co Seymchan meteorite as example materials. The latter was chosen as an intentionally challenging material for the alignments and it contains microstructural features on length scales of the order of interaction volumes of the measurement methods used.

2. Experimental procedure

Two different types of specimens were investigated in this study, an austenitic FeNiC (Fe-24Ni-0.4C) steel and a Seymchan meteorite (Fe-9.5Ni-0.5Co). The FeNiC steel represents a single-phase material, whereas the meteorite specimen was selected to represent a dual-phase material to demonstrate various correlation limitations.

The FeNiC steel and the meteorite samples were extracted with a size of about 1x1x0.5 cm^3, respectively, by electrical discharge machining or with a diamond saw. A metallographic preparation was then carried out to ensure an appropriately flat and deformation-free surface suitable for both, combined EBSD-EDS and nano-indentation experiments. Initially, the samples were mechanically ground and then polished using a water-based diamond suspension to a final 1 μm particle size. In order to minimise the surface relief which can affect the nano-indentation experiments, a short mechanical polishing was performed with 0.25 μm colloidal silica (OP-S, Struers, Denmark) on a neoprene polishing cloth (OP-Chem, Struers).

Microstructural analyses were performed by means of SEM, back-scattered electron (BSE) imaging and combined EBSD-EDS mapping in a dual-beam focused ion beam (FIB)-SEM Helios Nanolab 600i (FEI) (Hikari, EDAX Inc.) and a Hitachi SU-5000 in ETHZ ScopeM (Oxford UltimMax 100 EDS) at 20 kV. They were recorded with a step size of 1.3 μm across an area of 702x525 μm^2 for the steel and 1 μm step size across an 1280 × 769 μm^2 area for the Seymchan meteorite and were analysed using the EDAX OIM 7.3.1 software as well as the free MTEX 5.7.0 toolbox based on MATLAB® [20]. The EDS-mapping results were later quantified by the EDAX TEAM software using the e-ZAF method with binning option. The compositions of the austenitic FeNiC steel and the Seymchan meteorite based on preliminary studies and EDS investigations are shown in Table 1.

Nano-indentation experiments were performed on a FT-I04 Femto-Indenter (FemtoTools AG, Switzerland) equipped with an FT-S20,000 sensor and a diamond Berkovich tip. The indentation tests were performed in native displacement control to ensure a uniform maximum indentation depth for all indents. This also helps to control the inter-indent spacing to prevent strain field interactions and minimise the variations in elastic recovery between indents. The elastic portion of the recovery is determined through fast oscillation (150 Hz) of the indenter tip with a proportionally scaled oscillation amplitude. This continuous stiffness measurement (CSM) allows a stiffness measurement as a function of depth. For the two samples, the indentation depth and spacing were scaled relative to the microstructure of the samples. For the Seymchan meteorite fragment, a map of 384 by 216 indentations was performed with a maximum depth of 190 nm and a 2 μm spacing. For the austenitic FeNiC sample, a map of 250 by 200 indentations was carried out with a maximum depth of 95 nm and a 1 μm spacing. Representative values for each indentation were determined from the mean of values measured at contact depths above 50% of the target depth for elastic modulus and 80% for hardness to minimize errors from indentation size effects. By taking representative values at these relatively larger depths, influences from initial intermittent flow and indenter tip imperfection (observed at contact depths < 25 nm in this case) are avoided.

By NIT, the reduced modulus E_r is obtained and used to calculate the indentation modulus of the specimen E_{NI} considering the Poisson's ratio ν_S of the sample (Eq. (1)).

$$\frac{1}{E_r} = \frac{1-\nu_0{}^2}{E_0} + \frac{1-\nu_{S,isotropic}{}^2}{E_{NI}} \tag{1}$$

Eq. (1) is derived from the unloading stiffness in elastic deformation by a flat cylindrical punch of elastic materials [23,24], with the Young's modulus and Poisson's ratio for the diamond indenter, taken as E_0 =

Table 1
Reported and measured compositions in [wt.-%] of the austenitic steel and the Seymchan meteorite by means of EDS.

Specimen	Fe	Ni	Co	C	
FeNiC	Bal.	22.74		0.93 ± 0.2 [21]	Present study
Seymchan meteorite	Bal.	11.41 ± 0.24	0.48 ± 0.06		Present study
Seymchan meteorite	Bal.	9.5	0.5		[22]

1140 GPa and $\nu_0 = 0.07$, respectively.

The such measured indentation modulus is a weighted average of the material's single crystal elastic constants, where the weights depend on the crystal orientation, and are not necessarily the same for every indenter shape [19]. Later, it was shown that small deviations from a general axisymmetric indenter shape do not affect the obtained values of the indentation modulus, so that it is also applicable to Berkovich indenters [25] and elastic–plastic contact [26].

2.1. Point-to-point correlation

To achieve point-to-point correlations between nano-indentation, EBSD and EDS measurements, a dedicated Python library 'PyXC' was developed [57]. The library 'PyXC' corrects systematic distortions that occur with various measurement methods, aligns the data layers to a reference image and queries the data by an arbitrary x-/y-coordinate. In Fig. 1 the data query and the associated correlation procedure is depicted schematically.

Due to the flexibility of the library, almost any 2-dimensionally sampled data with or without x/y-coordinates can be correlated. However, to achieve the correlation without x/y-coordinate information (e.g. an image from an optical microscope or a scanning electron microscope) an assignment of missing x/y-coordinates based on respective pixel indices is required. Any data with x/y-coordinates can directly be loaded into the library.

In order to perform a point-to-point correlation, each layer must be accurately aligned. In general, this operation is difficult to automate since the representation of the data differs considerably between the various measurements, such that manual alignment is unavoidable. In some cases, the distortion of the collected data is of such complexity that the correction procedure cannot be achieved with simple translation and rotation operations due to the spatial distortion as demonstrated in Fig. 2. To deal with these distortions, either an affine transformation or homography is required. The transformation matrices for the 2-dimensional affine transformation and homography are given in Eq. (2) and Eq. (3), respectively [27].

$$\begin{bmatrix} x' \\ y' \\ 1 \end{bmatrix} = \begin{bmatrix} m_{11} & m_{12} & x_t \\ m_{21} & m_{22} & y_t \\ 0 & 0 & 1 \end{bmatrix} \begin{bmatrix} x \\ y \\ 1 \end{bmatrix} \tag{2}$$

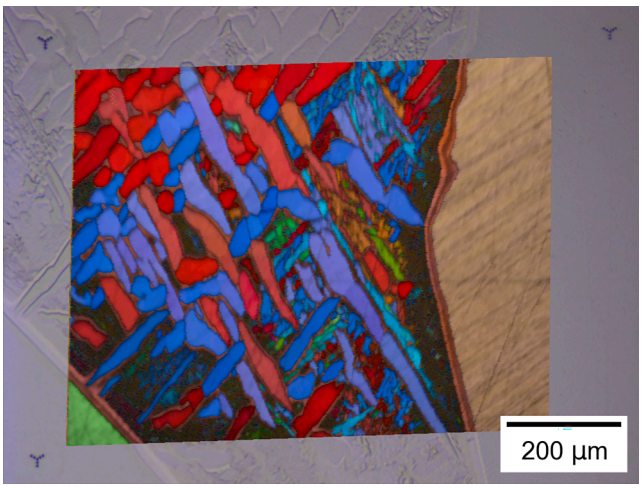


Fig. 2. Example of a spatially distorted EBSD map of the Seymchan meteorite calibrated using the 2-dimensional homography and aligned on top of an optical microscope image.

$$\begin{bmatrix} x' \\ y' \\ 1 \end{bmatrix} = \begin{bmatrix} h_{11} & h_{12} & h_{13} \\ h_{21} & h_{22} & h_{23} \\ h_{31} & h_{32} & 1 \end{bmatrix} \begin{bmatrix} x \\ y \\ 1 \end{bmatrix} \tag{3}$$

Here, x/y are an original point coordinate and x'/y' represent a new point coordinate after the transformation. The matrix components m_{ij} and h_{ij} denote the elements of the respective transformation matrix.

The correlation process is based on the evaluation of the Euclidean distance pairs. A schematic diagram that illustrates the point-to-point correlation process is given in Fig. 3. First, the distance between an arbitrary point x/y (e.g. from the nano-indentation layer) and all coordinates in the target layer (e.g. EBSD) is evaluated. Then, a calculated set of distance pairs is filtered out by a cut-off radius as well as the maximum nearest neighbour number. Values that are outside a certain cut-off radius around the query centre point (x,y) are not included in the correlation which reduces the computational costs to determine the Euclidean distance pair. Optionally, any statistical analysis (e. g. mean, standard deviation) can be performed for the experimental data points

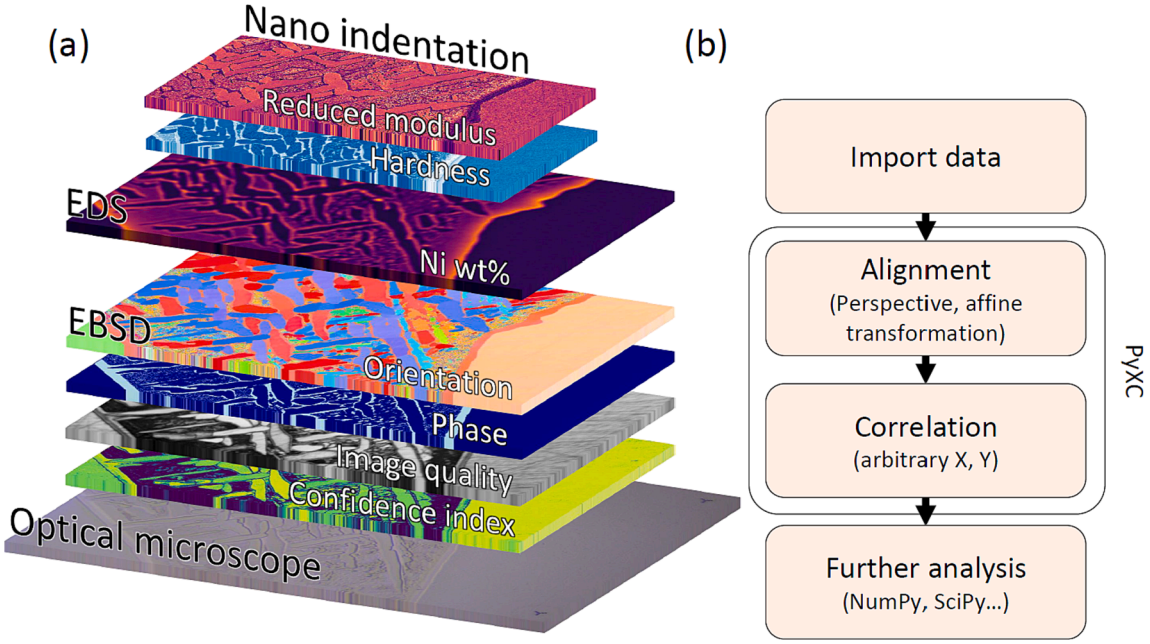


Fig. 1. (a) Schematic representation of the data query process on the example of the Seymchan meteorite data and (b) the methodological correlation procedure.

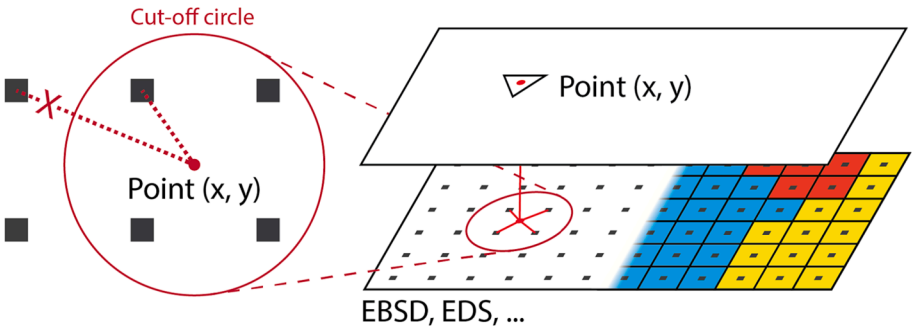


Fig. 3. Schematic diagram illustrating the point-to-point correlation process. Data points from the data layer can be obtained based on the Euclidean distance between the desired point locations.

that fulfil the cut-off condition (e.g. the 4 data points inside the red cut-off circle in Fig. 3). This correlation procedure is not only limited to nano-indentation and EBSD analysis, but also applicable for any 2-dimensionally sampled data.

Reading of the required scientific data such as EBSD, EDS, and nano-indentation was performed by a custom-developed in-house library and the IPF colouring was achieved by using the orix library [28]. Further analysis after the correlation step was realised with SciPy (least-squares and differential evolution minimisation) and the Scikit-learn (DBSCAN clustering) libraries, respectively [29,30].

2.2. Correlation with experimentally or DFT-based elastic moduli

A two-step procedure for predicting the single crystal stiffness tensor by correlated high-speed NIT, EBSD and EDS data is proposed. This approach begins with DFT-based (here using pure iron [31] to demonstrate the practicability, even if simplified initial data are used) interpolation of the optimised indentation moduli along (0 0 1), (0 1 1) and (1 1 1) planes normal directions. These indentation moduli are then applied in a second step to the mathematical relationship described by Vlassak and Nix to estimate the correct C_{11}, C_{12} and C_{44} values. A schematic representation of this procedure is shown in Fig. 4.

The estimation of the orientation-dependent indentation moduli begins with a point-to-point correlation of the EBSD, EDS and nano-indentation data, which relates crystallographic orientation to mechanical properties, resulting in sets of Euler angles, composition and indentation moduli. Here, the elastic modulus can be calculated in two ways. On the one hand, the nano-indentation based indentation modulus $E_{NI}(E_r, \nu)$ can be derived from E_r using Eq. (1) with the condition of $\nu = 0$ (according to V-N). On the other hand, the orientation-dependent elastic modulus $E_{OD}(C_{11}, C_{12}, C_{44}, \phi_1, \Phi, \phi_2)$ for the investigated cubic material can be calculated from the Euler angles (ϕ_1, Φ, ϕ_2)

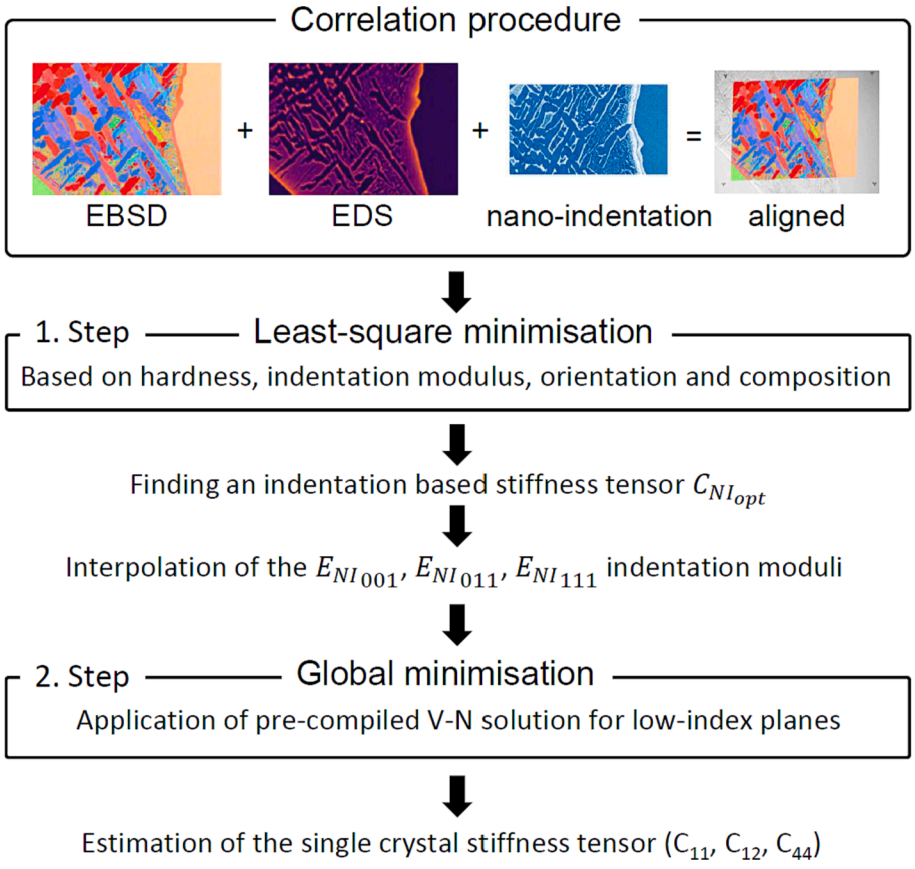


Fig. 4. Concept of the two-step estimation scheme.

and the stiffness tensor C in Voigt notation (in cubic crystal systems dependent on the elastic constants C_{11}, C_{12}, C_{44}) with Eq. (4).

$$\frac{1}{E_{OD}} = S_{11} - 2\left(S_{11} - S_{12} - \frac{S_{44}}{2}\right)\bullet\left(l_1^2 l_2^2 + l_2^2 l_3^2 + l_1^2 l_3^2\right) \tag{4}$$

S_{ij} denote the independent entries of the elastic compliance matrix obtained from the stiffness tensor, while l_1, l_2 and l_3 represent the direction cosines for an arbitrary crystallographic direction l which can be calculated from the rotation matrix R_{ZXZ} (according to Bunge) that is described in Eq. (5).

$$R_{ZXZ} = R_Z(\theta) \bullet R_X(\theta) \bullet R_Z(\theta) \text{ with } R_Z(\theta) = \begin{bmatrix} cos\theta & -sin\theta & 0 \\ sin\theta & cos\theta & 0 \\ 0 & 0 & 1 \end{bmatrix} \text{ and } R_X(\theta) = \begin{bmatrix} 1 & 0 & 0 \\ 0 & cos(\theta) & -sin(\theta) \\ 0 & sin(\theta) & cos(\theta) \end{bmatrix} \tag{5}$$

With the given E_{OD} and E_{NI} values, it is possible to perform a least-squares optimisation to find out the best C_{11}, C_{12}, and C_{44} values which describe the optimised indentation-based stiffness tensor $C_{NI_{opt}}$. For this purpose, the least-squares optimiser minimises the cost function given in Eq. (6). The cost function F equals the sum of absolute differences between E_{OD} and E_{NI}.

$$F = \sum_i |E_{OD,i} - E_{NI,i}| \tag{6}$$

However, since there are several local minima, a proper initial guess is crucial to ensure a reliable solution. The initial values for the elastic constants C_{11}, C_{12}, and C_{44} can be set by either available experimental ($C_{exp_{initial}}$) or DFT-based ($C_{DFT\,initial}$) data. In this study data for pure iron from DFT was used [31].

Before, it was necessary to accurately determine the indentation moduli along the (0 0 1), (0 1 1), (1 1 1) planes normal directions experimentally for this solution, which is not always possible, particularly if the exact crystal orientations are not contained in a polycrystalline sample of interest. However, based on the proposed approach, the indentation moduli along the (0 0 1), (0 1 1), and (1 1 1) planes normal directions, respectively $E_{NI(001)}$, $E_{NI(011)}$, and $E_{NI(111)}$, were interpolated from the optimised $C_{NI_{opt}}$. Subsequently, these specific indentation moduli could be applied to the V-N solution for cubic materials (Eq. (7) [19]), eliminating the need for indentation tests in these specific low-index planes.

$$E_{NI\,(hkl)} = \beta_{(hkl)}\left(\frac{E}{1-\nu_{VRH}^2}\right)_{isotropic} \tag{7}$$

The correction factor β is given by Eq. (8) [19].

$$\beta = a + c(A - A_0)^B = a + c\left(\frac{2C_{44}}{C_{11} - C_{12}} - A_0\right)^B \tag{8}$$

The terms a, c, A_0 and B denote fitting parameters which are valid for a fixed Poisson's ratio $\nu_{<001>}$ in the $\langle 0\,0\,1\rangle$ direction (Eq. (9)) given in the V-N model [19] and the term A reflects the Zener ratio (often referred to as anisotropy factor) according to Eq. (10) [32].

$$\nu_{<001>} = -\frac{S_{12}}{S_{11}} \tag{9}$$

$$\mathrm{A} = \frac{2C_{44}}{C_{11} - C_{12}} \tag{10}$$

The elastic modulus can be calculated from the stiffness tensor C_{ij} and its compliance tensor S_{ij} using the Voigt-Reuss-Hill (VRH) average [33], where the respective Voigt [34] and Reuss [35] arithmetic averages of the bulk and shear moduli are taken into account. The VRH-average of the elastic modulus is given by Eq. (11).

$$E_{VRH} = \frac{9K_{VRH}G_{VRH}}{3K_{VRH} + G_{VRH}} = \frac{\overbrace{3(c_{11}+2c_{12})}^{9K_{VRH}}\overbrace{\left(\frac{3\,c_{11}^2 - 6\,c_{11}c_{12} + 3\,c_{12}^2 + 38\,(c_{11}-c_{12})c_{44} + 12\,c_{44}^2}{10\,(3\,c_{11} - 3\,c_{12} + 4\,c_{44})}\right)}^{G_{VRH}}}{\underbrace{(c_{11}+2c_{12})}_{3K_{VRH}} + \underbrace{\left(\frac{3\,c_{11}^2 - 6\,c_{11}c_{12} + 3\,c_{12}^2 + 38\,(c_{11}-c_{12})c_{44} + 12\,c_{44}^2}{10\,(3\,c_{11} - 3\,c_{12} + 4\,c_{44})}\right)}_{G_{VRH}}} \tag{11}$$

From isotropic elasticity theory, the Poisson's ratio of a given crystal can be calculated from the respective averaged shear and bulk moduli according to Eq. (12).

$$\nu_{\ VRH} = \frac{3K_{VRH} - 2G_{VRH}}{2(3K_{VRH} + G_{VRH})} = \frac{\overbrace{c_{11} + 2\,c_{12}}^{3K_{VRH}} - \overbrace{\frac{3\,c_{11}^2 - 6\,c_{11}c_{12} + 3\,c_{12}^2 + 38\,(c_{11}-c_{12})c_{44} + 12\,c_{44}^2}{5(3\,c_{11} - 3\,c_{12} + 4\,c_{44})}}^{2G_{VRH}}}{\underbrace{2\,c_{11} + 4\,c_{12}}_{6K_{VRH}} + \underbrace{\frac{3\,c_{11}^2 - 6\,c_{11}c_{12} + 3\,c_{12}^2 + 38\,(c_{11}-c_{12})c_{44} + 12\,c_{44}^2}{5(3\,c_{11} - 3\,c_{12} + 4\,c_{44})}}_{2G_{VRH}}} \tag{12}$$

In order to estimate the single crystal stiffness tensor, a global minimisation [30] was performed based on Eq. (13) as well as Eq. (14) and the relating cost function Eq. (15).

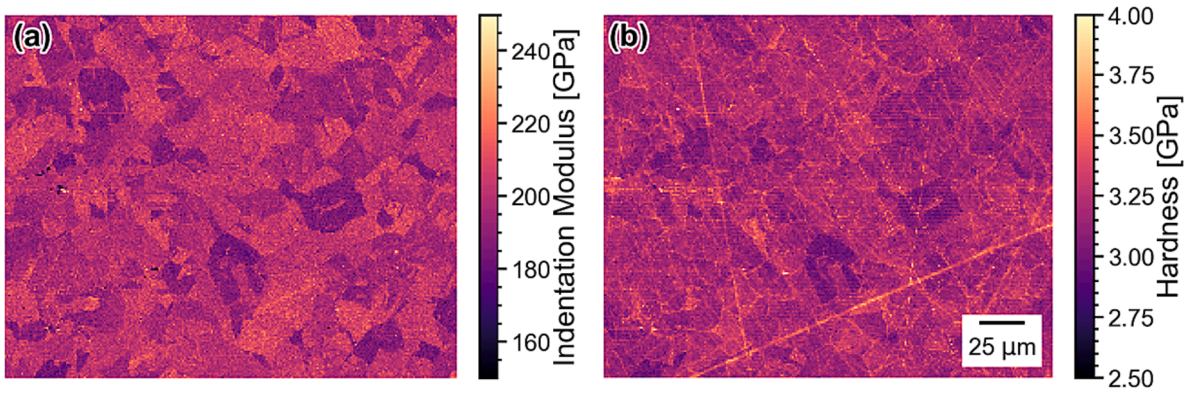


Fig. 5. (a) Indentation modulus map and (b) hardness map of the austenitic FeNiC steel. The lines indicate locally work-hardened sub-surface deformation zones caused by initial scratches resulting from metallographic preparation.

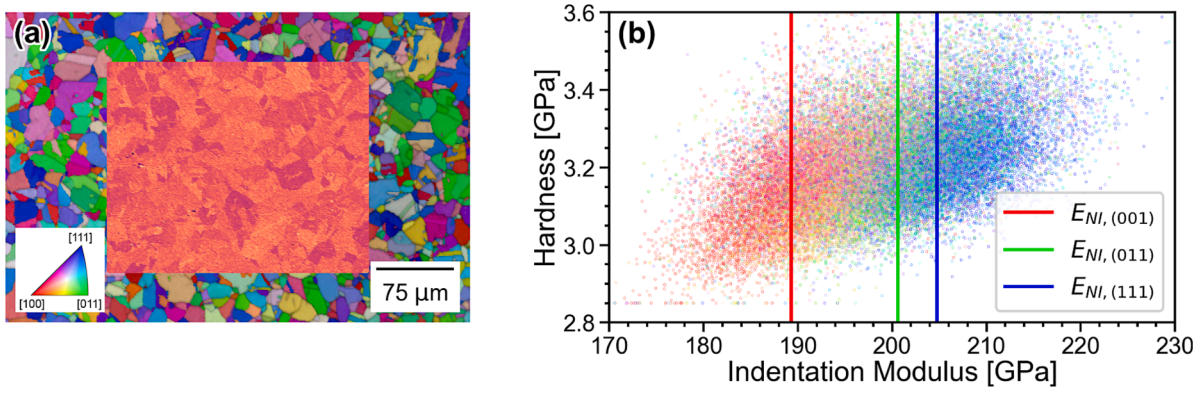


Fig. 6. (a) EBSD with the indentation mapped area indicated and (b) orientation-dependent hardness vs. indentation modulus plot of the austenitic FeNiC steel sample coloured with respect to crystal orientation and predicted indentation moduli along the (001), (011) and (111) planes normal directions.

$$F_{(hkl)}(C_{11}, C_{12}, C_{44}) = \beta_{(hkl)} \left(\frac{E_{VRH}}{1 - \nu_{VRH}^2} \right)_{isotropic} - \overbrace{E_{NI(hkl)}}^{from\ 1.\ Step} \quad for\ hkl = 001,\ 011\ and\ 111 \tag{13}$$

$$F_{\nu} = \nu_{<001>_{proposed}} - \nu_{<001>} \tag{14}$$

$$F_c = |F_{(001)}| + |F_{(011)}| + |F_{(111)}| + |F_{\nu}| \tag{15}$$

Using this approach with these preconditions and solely being dependent on the elastic constants C_{11}, C_{12} and C_{44}, a global minimum could be estimated and predict the stiffness tensor taking into account the pre-compiled fitting parameter sets for a proposed Poisson's ratio in ⟨001⟩ direction $\nu_{<001>_{proposed}}$(FeNiC = 0.35 / Seymchan meteorite = 0.3) based on the V-N method.

3. Results

3.1. Single phase material - FeNiC steel

3.1.1. Alignment between EBSD/nano-indentation data and first assessment of the single crystal stiffness tensor by the two-step approach

The crystallographic orientation significantly affects the local elastic response. Correlative nano-indentation and EBSD measurements were applied to reveal the orientation-dependent elastic properties. High-speed NIT maps on the FeNiC steel are presented in Fig. 5 for the measured indentation modulus and hardness. These clearly display the underlying grain structure beneath the sample surface, which correlates well with the EBSD results, as shown in Fig. 6a). Some scatter can be observed in the indentation modulus map, which can be a function of either subsurface damage from imperfect surface preparation, remnant roughness [36] or local variations in dislocation density in cold-worked materials. The former is more likely in this case, as illustrated by the subsurface deformation zones or 'scratches' noticeable in the hardness map in Fig. 5b). Due to the larger size of the elastic strain field from which the indentation modulus is measured, relative to the plastic strain field measured by hardness, the effect of subsurface damage on the data is significantly less pronounced in the indentation modulus map than the hardness map.

E_{OD} was calculated assuming a samplés Poisson's ratio of 0, resulting in sets of correlated indentation modulus, hardness and orientation information. The orientation-dependent hardness and indentation modulus (E_{NI}) distribution of the indented area from Fig. 6a) as well as the predicted specific indentation moduli along the (001), (011) and (111) planes normal directions (Table 2) are presented in Fig. 6b).

As a first step, a least-squares optimisation technique (Sec 2.2) was applied to find the optimal C_{11}, C_{12} and C_{44} values that best predict the orientation-dependent indentation modulus. An initial stiffness tensor C was optimised, here taking into account $C_{DFT\,initial}$(Fe) of pure iron [31] and E_{NI} (Sec 2.2). By applying the resulting optimised $C_{NI_{opt}}$ entries, the directional indentation moduli at each data point were predicted using the related Euler angles with Eq. (4). The visualisation of the predicted, direction-dependent indentation modulus following the optimisation

Table 2
Least-squares fitted indentation moduli for the (001), (011) and (111) planes, respectively.

E_{NI001}	E_{NI011}	E_{NI111}
189.3 GPa	200.6 GPa	204.7 GPa

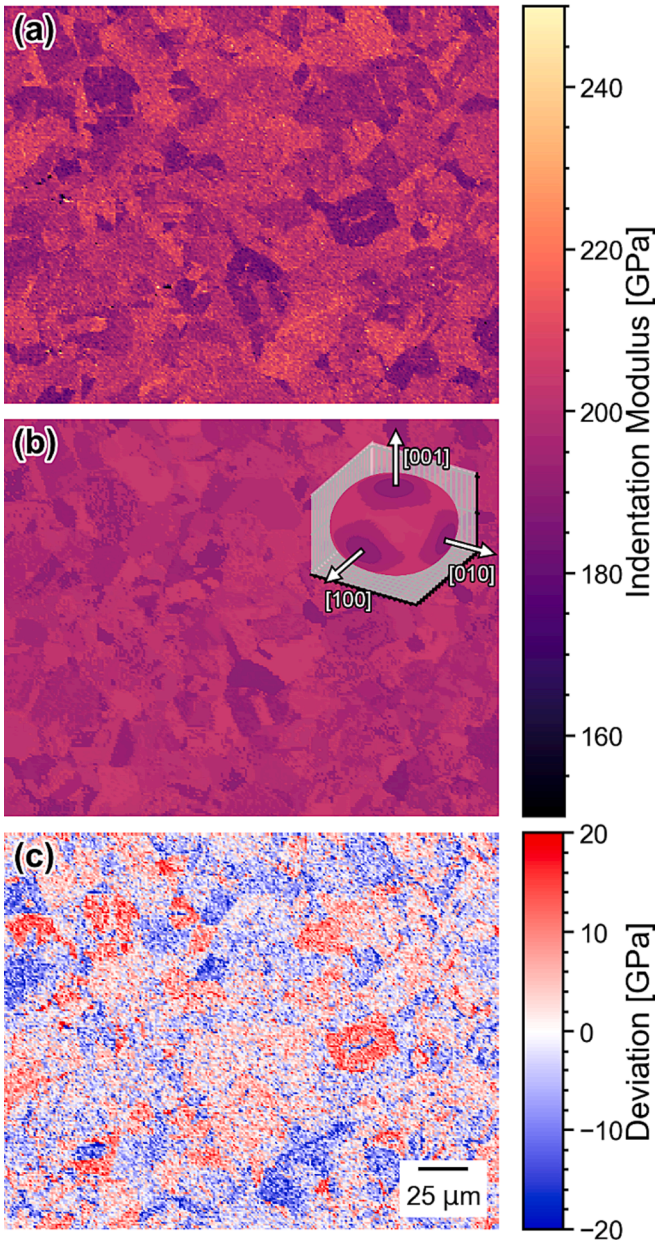


Fig. 7. First optimisation step using the austenitic FeNiC steel data showing (a) the experimentally obtained indentation modulus, (b) the predicted directional indentation moduli and the underlying spatial representation of $C_{NI_{opt}}$ visualised as inset in cartesian coordinates aligned with the [0 0 1] axes of the unit cell; (c) the differences between the predicted indentation modulus and the experimentally obtained indentation modulus.

procedure is illustrated in Fig. 7. In the first optimisation step the indentation modulus could be reproduced with good accuracy (average deviation = ±6 GPa), as shown in Fig. 7a) and Fig. 7b).

A second global minimisation step allowed further refinement of the obtained indentation modulus for low index planes in order to predict the single crystal stiffness tensor. For this purpose, the indentation moduli of the specific planes were determined on the basis of the first optimisation step using Eq. (7) and are presented in Table 2.

The values of the resulting indentation moduli and stiffness tensors $C_{NI_{opt}}$ and $C_{NI_{opt2}}$, respectively, are given in Table 3.

The tensor-based approach is particularly useful when the measurements ideally involve high-speed NIT, as it provides good statistics. However, it can also be useful in cases where there is no possibility to specifically measure different crystallographic planes or different sized data sets are to be correlated. As demonstrated using a subset of the steel sample in Fig. 8, the converged value of the $C_{NI_{subset}}$ exhibited similar values compared to the full dataset refinement if a good grain orientation distribution is ensured, as shown in Table 4.

3.2. Multi-phase material - Seymchan meteorite

3.2.1. Layer alignment for optical microscopy, EBSD, EDS and hardness data

The Seymchan meteorite sample was used in order to demonstrate the combined capabilities and limitations of the correlation procedure. In the present investigation, a plessite region that comprises a fine mixture of body-centered-cubic kamacite (referred to hereafter as α_m) and thin seams of taenite/ tetrataenite (referred to hereafter as γ_m) around the α_m grains was studied [27]. In addition, fine-grained intermediate domains of α_m and γ_m are visible. The mechanical properties within the plessite region were investigated using high-speed NIT and are also discussed in terms of the multimodal alignment of the correlated methods in Sec. 4.2. In Fig. 9 the indentation area of the analysed microstructure is shown using optical microscopy (Fig. 9a)) with aligned EBSD, EDS and hardness data given in Fig. 9b).

The mechanical properties of the corresponding region of the meteorite sample were plotted in the hardness-indentation modulus space (Fig. 10). The α_m and the γ_m clusters were visually determined by a correlation with EBSD/EDS phase information, which are indicated in Fig. 10a) and Fig. 10b) exhibiting the respective mechanical properties. In between these clusters, an intermediate zone is revealed and a clear orientation dependence can be observed for the α_m region. However, the orientation dependence of the other regions is not clearly visible. Furthermore, the cross-contamination between α_m and γ_m due to residual misalignment of the data should also be removed as far as possible (which will be discussed in detail in Sec. 4).

In order to facilitate the consecutive investigation of the orientation-dependent elastic response data on the meteorite sample, it is necessary to appropriately filter the correlated nano-indentation data based on the aligned microstructural information to isolate the α_m cluster.

The application of filtering techniques based on the confidence index, EBSD phase information, and DBSCAN clustering enable the exclusion of phases such as γ_m and the intermediate zone. Thereby, a further analysis solely on the α_m phase can be performed using the least-

Table 3
Initial and optimised DFT/indentation-based elastic constants as well as Zener ratio with varying Poisson's ratios and experimental data from the literature.

Ni	C	C_{11}	C_{12}	C_{44}	E_{VRH}	Zener ratio	ν_{VRH}	$\nu_{<001>}$	Reference
[wt%]		[GPa]							
0	0	266.63	122.63	104.5	229.7	1.45	0.28	0.32	Pure Fe [31] (Initial values from DFT)
24	0.4	246.3	99.2	80.6	198.4	1.10	0.28	0.29	1st optimisation ($C_{NI_{opt}}$ tensor)
24	0.4	199.8	107.5	87.7	174.7	1.90	0.29	0.35	2nd optimisation ($C_{NI_{opt2}}$ tensor)

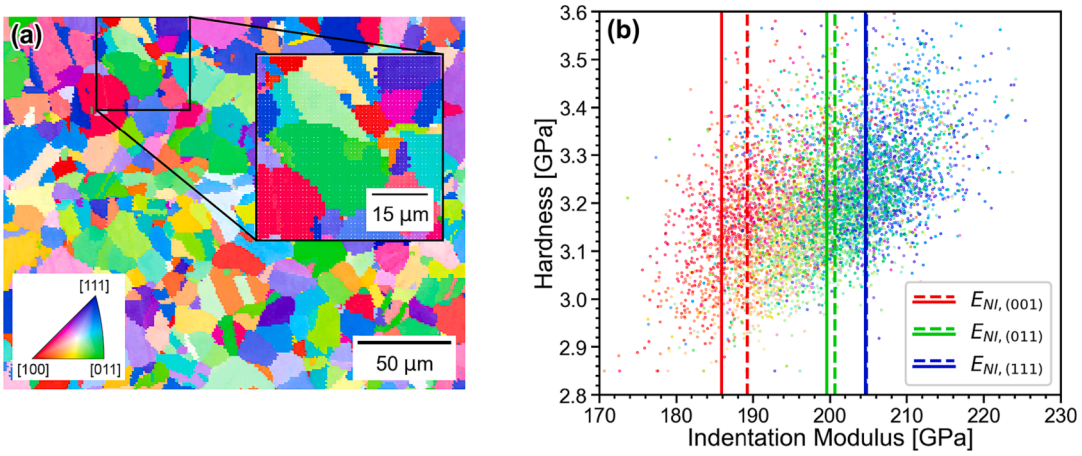


Fig. 8. (a) Location and (b) data distribution of a selected subset region of the austenitic steel data highlighting the predicted indentation moduli for the specific (0 0 1), (0 1 1) and (1 1 1) planes as vertical lines. The dashed lines represent the predicted indentation moduli of the entire map for comparison.

Table 4
Total (grain size filtered > 20) data set compared to a subset used for optimisation. The estimated single crystal stiffness tensor components exhibit similar values when the subset contains sufficient grains with orientations spanning the full orientation range.

Sample	No. of points	No. of grains	$C_{11\,opt^2}$	$C_{12\,opt^2}$	$C_{44\,opt^2}$
FeNiC (full)	49,800	approx. 400	199.8	107.5	87.7
FeNiC (subset)	2369	approx. 25	186.0	100.1	92.7

squares method described in Sec 2.2.

The consequence of the used filtering operations is illustrated in Fig. 11. In the present study, the contributions from the intermediate zone (depicted in Fig. 10a)) and the γ_m phase were removed by applying a sequence of filtering. This procedure is covered and discussed in more detail in Sec. 4.2.

Using this approach, it is possible to estimate the angular dependent indentation modulus E_{NI} by the optimised $C_{NI\,opt}$ based on a stiffness tensor $C_{DFT\,initial}(Fe)$ as shown in Fig. 12. The predicted E_{NI} (Fig. 12b)) was found to reproduce E_{NI} (Fig. 12a)) accurately.

4. Discussion

In this study, a method for the estimation of the orientation-dependent indentation modulus and the subsequent estimation of the single crystal stiffness tensor using correlative multi-modal investigations is described. For this purpose, measurement modalities including EBSD, EDS, nano-indentation and first-principle investigations were correlated in order to combine orientation, composition and indentation information using a newly developed Python library "PyXC". Based on a least squares minimisation, by using either initial experiment- or DFT-based stiffness tensors, the best fitting values for the orientation-dependent indentation modulus tensor $C_{NI_{opt}}$ could be estimated. Further, $C_{NI_{opt}}$ was used to obtain predictions of the indentation moduli along the (0 0 1), (0 1 1) and (1 1 1) planes normal directions in order to estimate the complete stiffness tensor of the single crystal from these indentation moduli determined on the basis of the V-N solution for cubic materials.

Previously, the evaluation of the constitutive equations could be performed using the V-N model to achieve accurate results for most indentation experiments. However, a solution of these constitutive equations from the V-N model is not available analytically. Consequently, computationally intensive numerical simulations are often required and their evaluation is difficult for many researchers using nano-indentation experiments.

The method proposed in this study enables an estimation of the single-crystal stiffness tensor without solving the V-N model by using pre-compiled solutions for cubic materials. Using the examples of a single phase austenitic FeNiC steel and a two-phase nickel-bearing Seymchan meteorite, the capabilities, limitations and methods for overcoming the deficiencies of the newly developed combinatorial analysis are demonstrated.

4.1. FeNiC steel

Qualitatively, the mechanical properties that are revealed by the indentation maps are consistent with earlier observations by Vlassak and Nix as well as other observations [11,19]. Here, the indentation modulus of the (1 0 0) plane is the lowest, while for the (1 1 1) plane it is the highest. Furthermore, the measured hardness values of the sample showed a different degree of variation over the varying orientations. However, most importantly, the indentation moduli were predicted reasonably from the indentation modulus tensor as shown in Table 2 and illustrated in Fig. 6b).

In the second optimisation step, the C_{11}, C_{12}, C_{44} values of the single crystal stiffness tensor were estimated by applying the pre-compiled solutions of the V-N model. The optimised $C_{NI_{opt^2}}$ entries resulting from the second optimisation is compared with other experimental results [37] in Fig. 13 revealing a good agreement.

Overall, the tensor-based two-step approach yielded good results and it is particularly useful when high-speed NIT is involved, as it provides good statistics for applying the least-squares optimisation.

4.2. Seymchan meteorite

In general, correlation is particularly difficult if there is insufficient statistical data or if it is performed on multi-phase materials. The difficulties are demonstrated here using a dual phase meteorite as an example. The correlation of the meteorite sample was challenging for the following reasons: (i) the contribution from regions of no interest must be properly filtered out to avoid cross-contamination, (ii) the relatively coarse grain size did not provide a good grain orientation distribution, (iii) the grain size difference and complex grain boundary regions between the α_m and γ_m made alignment difficult, (iv) the indentation spacing was similar-sized to the fine-scale features in the microstructure, (v) indentations placed on lateral or subsurface interfaces between phases yield mixed results. Hereinafter these limitations will be referred to as filtering, statistics or alignment problem, respectively.

The combination of nano-indentation and microscopy-based analysis provides the possibility of a complex filtering process to exclude any

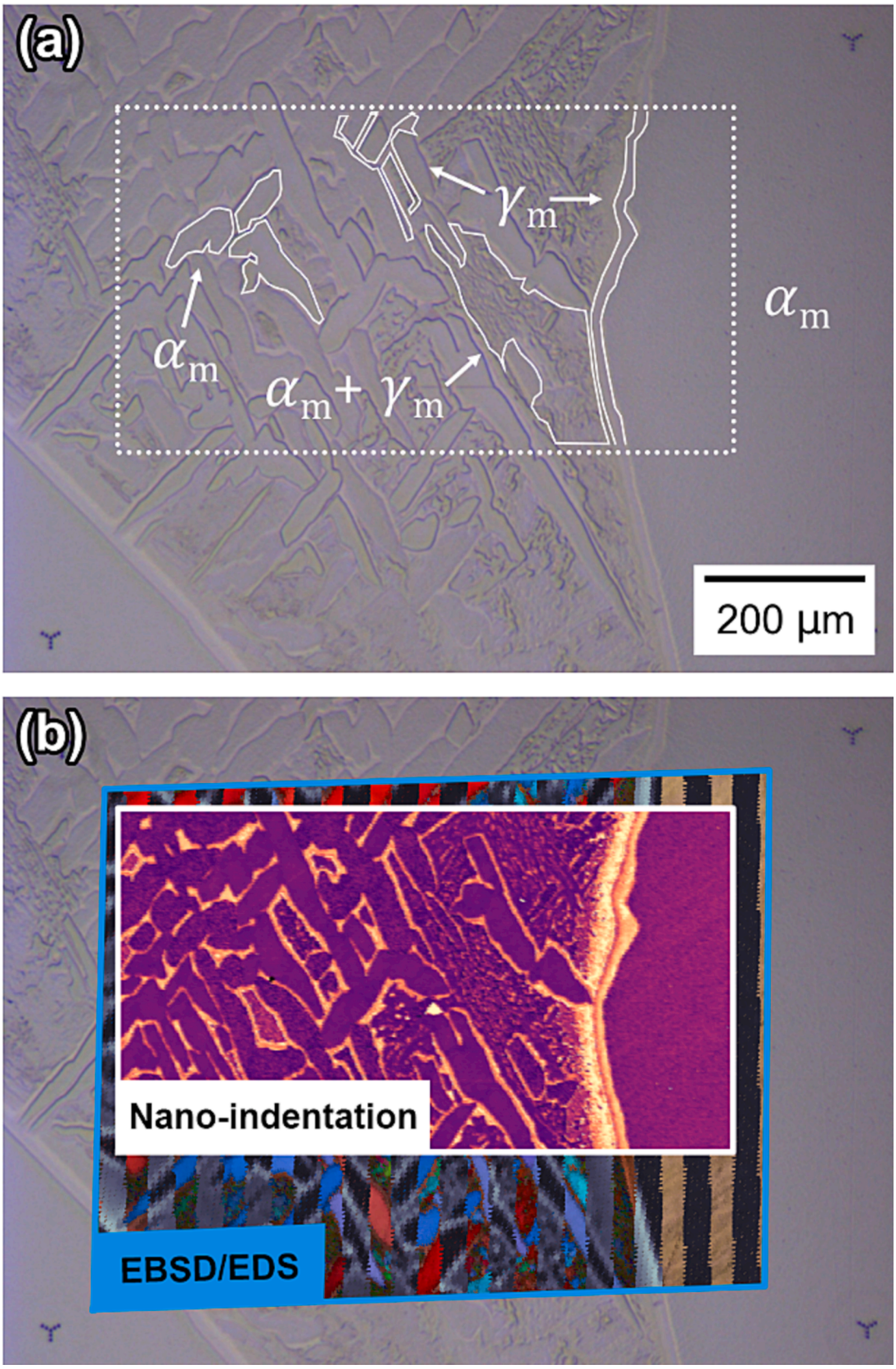


Fig. 9. (a) Optical microscopy of the region of interest in the plessite region of the Seymchan meteorite and (b) alignment result for the optical micrograph, EBSD, EDS and hardness data.

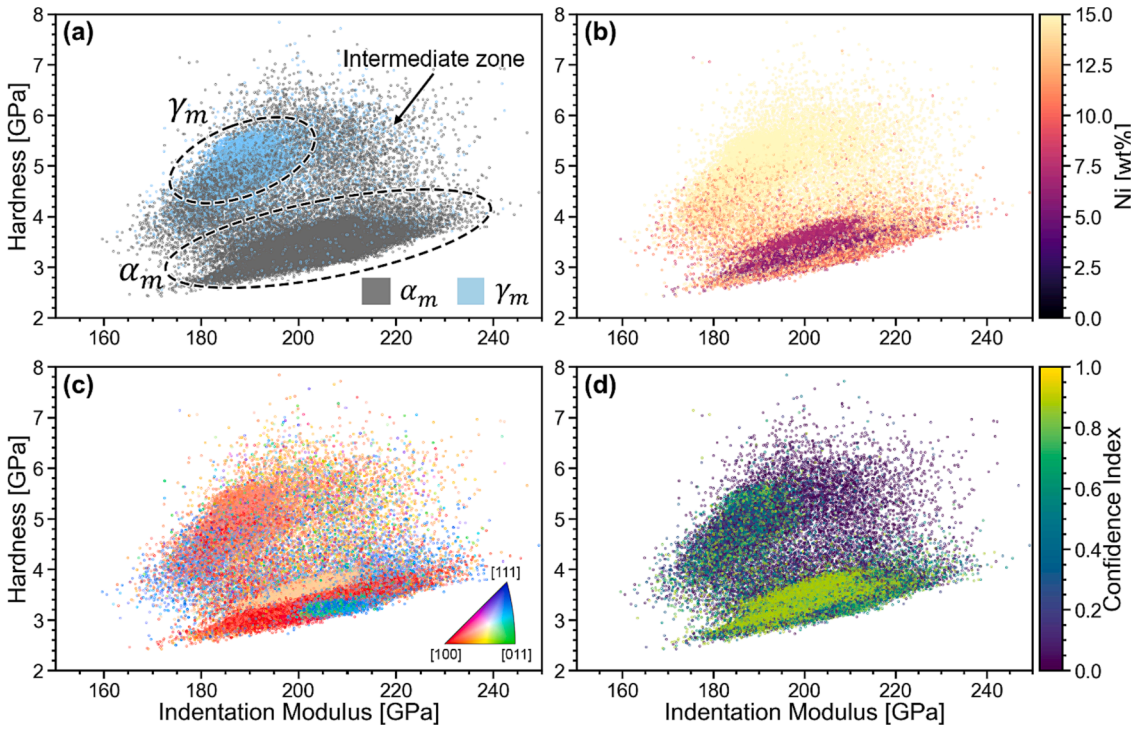


Fig. 10. Hardness vs. indentation modulus plots of the Seymchan meteorite sample showing (a) phase separation, (b) nickel content from aligned EDS data, (c) IPF coloring from aligned EBSD data (the green [0 1 1] orientations are intentionally plotted in the foreground for better visualization) and (d) confidence index values from aligned EBSD data.

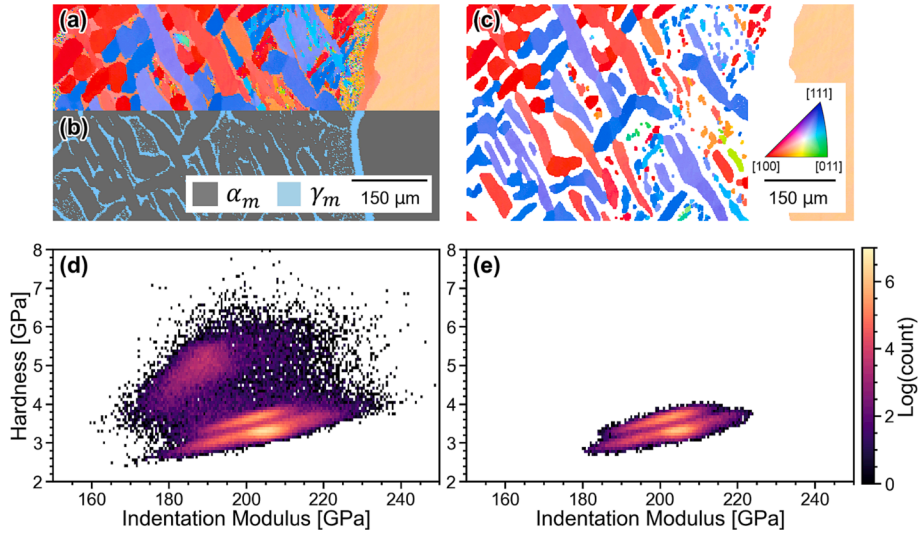


Fig. 11. Filtering procedure applied for the Seymchan meteorite to enable separate analysis of the α_m phase. EBSD data filled by nearest-neighbour approach (a) before combination with a (b) phase map and (c) after filtering. (d) Unfiltered and (e) filtered intensity plots for the Seymchan meteorite.

undesired phase, but it depends strongly on the material system and is therefore very individual. As the Seymchan meteorite consists of a complex microstructure, it requires appropriate filtering for further correlation. By combining several filtering conditions, the contribution from γ_m and the fine-grained mixture region were removed. First, the EBSD-based phase filter (phase = kamacite) was applied to extract the γ_m, but due to misalignment, covered later in this section, the γ_m could not be fully filtered out. Therefore, by applying a composition based (Ni wt% $<$ 10 wt%) and a confidence index filter (CI $>$ 0.5), almost all contributions from the γ_m phase were successfully removed. As a final processing step, a DBSCAN clustering with a minimum cluster size of 50 data points and a maximum distance of 0.08 between the data points was applied to eliminate data points with a large predefined distance to the cluster. This series of filtering operations as depicted in Fig. 14 was used to determine the mechanical responses of the correlated pure α_m phase.

4.2.1. *Grain orientation statistics*

A challenge resulting from a lack of grain orientation statistics is that a frequent occurrence of the specific crystallographic orientations can bias the least squares minimisation. For example, in Fig. 15, the predicted indentation moduli along the (0 0 1) and (1 1 1) planes normal

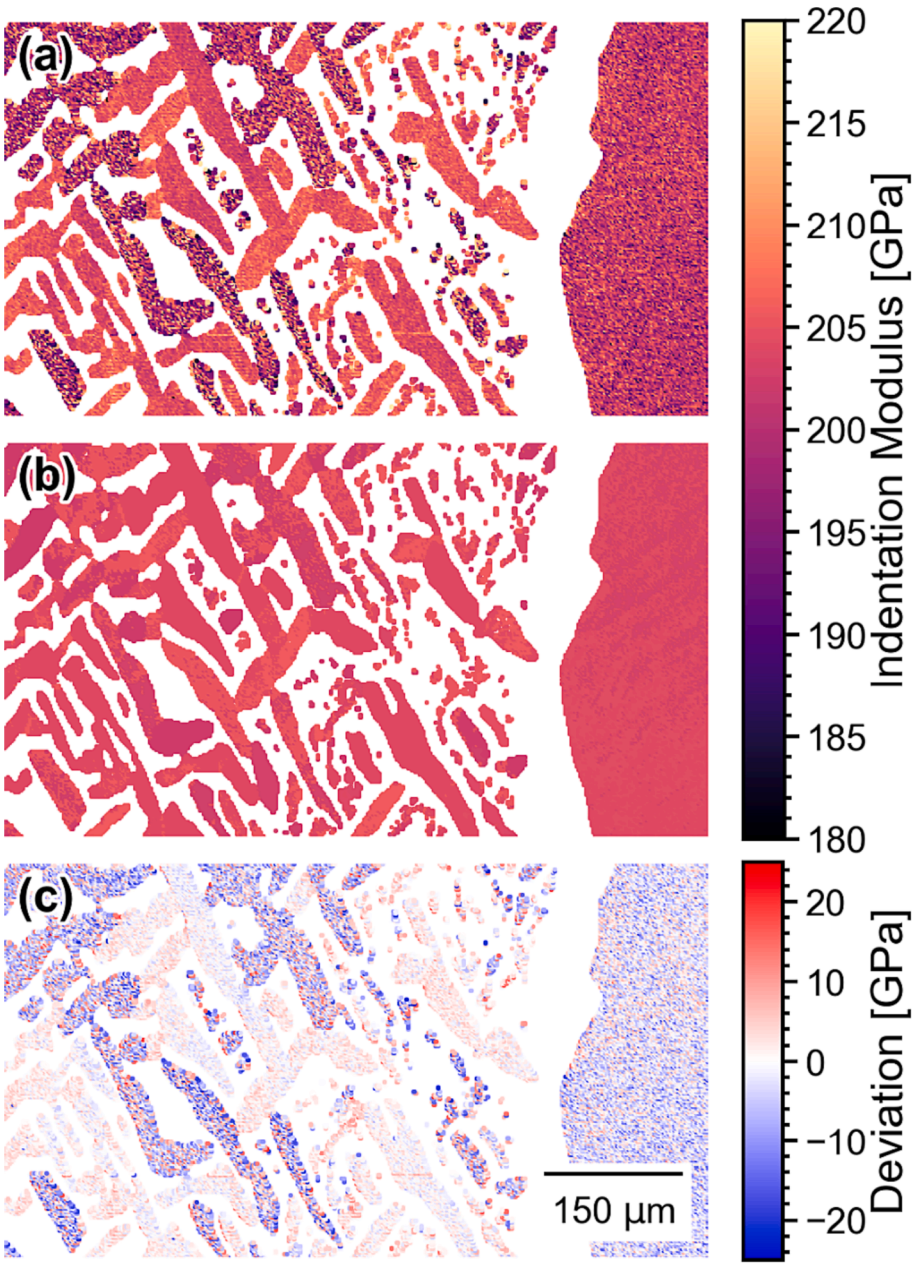


Fig. 12. (a) E_{NI} calculated from experimental E_r using a Poissońs ratio of$\nu = 0$, (b) predicted E_{NI} from $C_{NI_{opt}}$ for the α_m phase of the Seymchan meteorite and (c) deviation between (a) and (b).

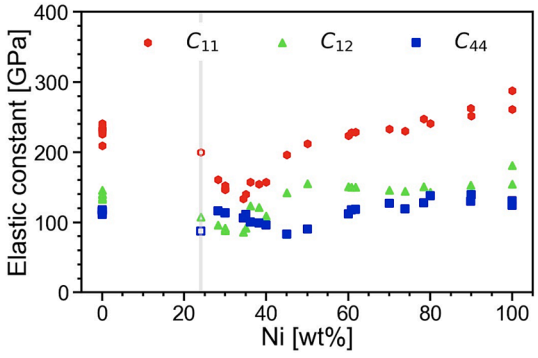


Fig. 13. Single crystal elastic constants from different pulse-echo-overlap measurements (Fe-Ni) [37–52] compared with the predicted values for the FeNiC derived from the two-step method presented in this study.

directions are well identified, as they are represented well by measurements on grains oriented accordingly, but the indentation modulus of the (0 1 1) plane could not be verified easily.

In this case for the Seymchan meteorite, the validation of the predicted indentation modulus of the (0 1 1) plane is not well achievable due to the relatively small number of orientations near the (0 1 1) plane, as shown in Fig. 11c). As a result, it is not possible to determine or confirm the indentation modulus of the (0 1 1) plane with certainty, which could be improved by a more homogeneous orientation distribution, e.g. by measuring across several areas or generally a larger area if the overall texture is not too strong. Most measurements were taken on grains with a surface plane near (0 0 1) and (1 1 1). Greater deviations from the predicted modulus are present in the near (0 0 1) orientations, as indicated by the purple colouring in Fig. 12c) as a result of a mix of larger deviations from the predicted value towards the red and blue ends of the colour scheme. This is related to the wider distribution around the average value in these grains visible in Fig. 15. It occurs with a

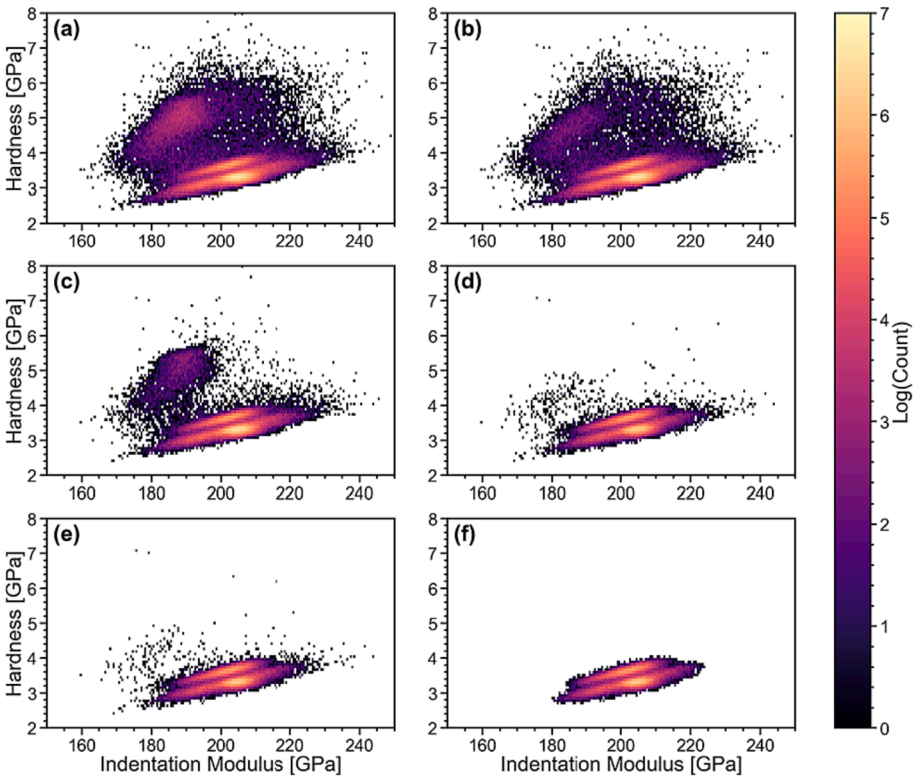


Fig. 14. (a) Raw data set without filtering and (b)-(f) sequential filtering steps to reveal respective filter effects. (b) Phase (here Kamacite), (c) CI (here > 0.5), (d) composition (here Ni < 10 wt%), (e) combined (here Phase + CI + composition) and (f) refined clustering (here DBSCAN) + combined filter methods.

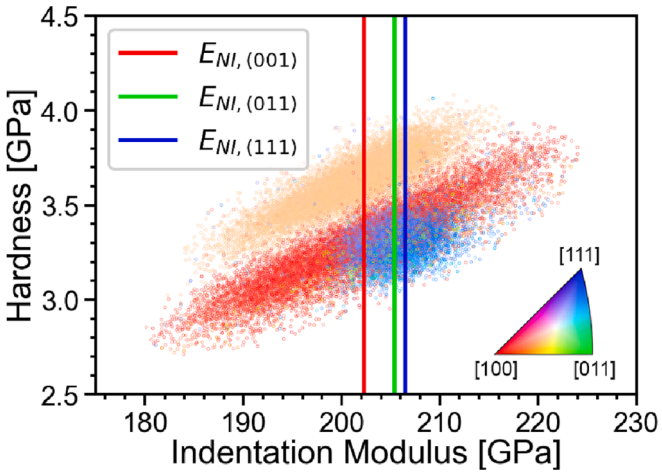


Fig. 15. Hardness vs. indentation modulus plot for the Seymchan meteorite, colourised according to the corresponding orientations (IPF colour code) and highlighted predicted indentation moduli for the three specific crystallographic planes (001), (011) and (111), respectively.

systematic relationship between hardness and modulus in the sense of a constant H/E and this phenomenon does not appear to be related to a local gradient in Ni concentration as shown in Fig. 10b). It is, however, correlated with a stronger variation in surface height as extracted from the contact height measurements during indentation. It is therefore assumed that the increased scatter of the modulus mapping at constant ratio H/E originates from an orientation dependent etching topography encountered in this meteorite phase during the last metallographic preparation steps. Clarification of the origin of the orientation dependent etching and its exact nano-scale morphology are beyond the scope of this work, but are in principle well documented in the literature for different materials [53] and also used for crystal orientation mapping [54].

4.2.2. *Alignment and interpretation of data sets with small features*

For the microstructure of the meteorite sample, the most difficult part is the alignment. In Fig. 10 it can be seen that the γ_m region does not only consist of γ_m points. It also contains a certain amount of α_m points. This is due to the challenges anticipated and indeed presented by this microstructure. The existence of two phases and small single phase regions makes alignment much more challenging than in a single phase polycrystal, as long as the grain size is significantly larger than the minimum indentation spacing. In addition, near the interphase boundary, even small misalignments can make the correlated data inaccurate. Furthermore, the orientation, chemical and mechanical analyses suffer from averaging effects related to their respective interaction volumes (visualised indirectly in terms of the EBSD confidence index (CI) in Fig. 10d)) as well as possible distortions in the signal due to surface topography originating from the metallographic preparation and mechanical contrast between the phases. For the thin γ_m phase, in contrast to the bulky α_m phase, the major part of the data is visibly contaminated by α_m due to the misalignment.

Although the two-dimensional correlation technique has proven to be quite serviceable, correlative nano-indentation is challenging under special circumstances. Several of these issues for single phase materials have already been discussed in detail by Magazzeni et al. for the XPCorrelate tool which provides similar capabilities within the MATLAB® environment [17]. The limitations were divided into two categories, alignment and interpolation, where the alignment limitation originated from misalignment of the different measurements, while the interpolation limitation resulted from interpolation between the datasets with different data characteristics.

The correlation between the different datasets requires consideration of the limitations of the respective measurement methods. For example, high-speed NIT can be less precise than classical nano-indentation due

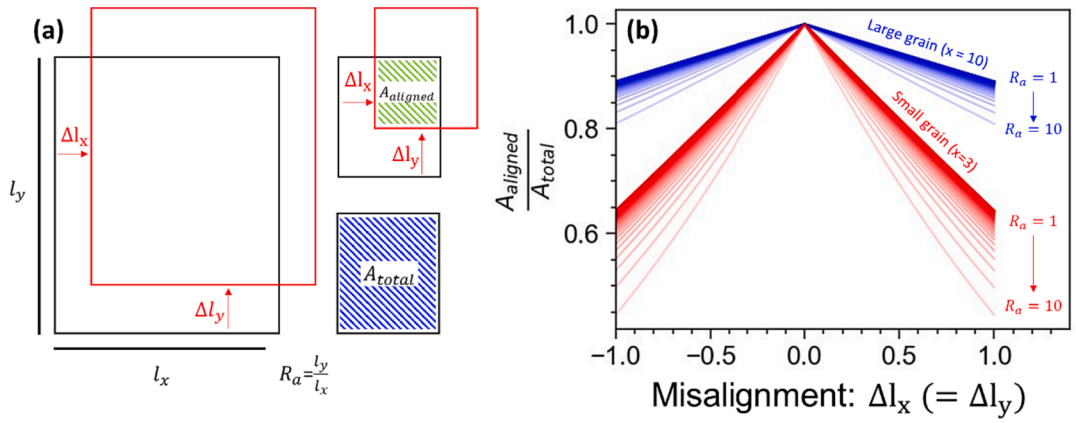


Fig. 16. (a) Assumed geometries with similar aspect ratio, but different sizes for (b) calculation results of the fraction of the correctly aligned area depending on the grain/area size.

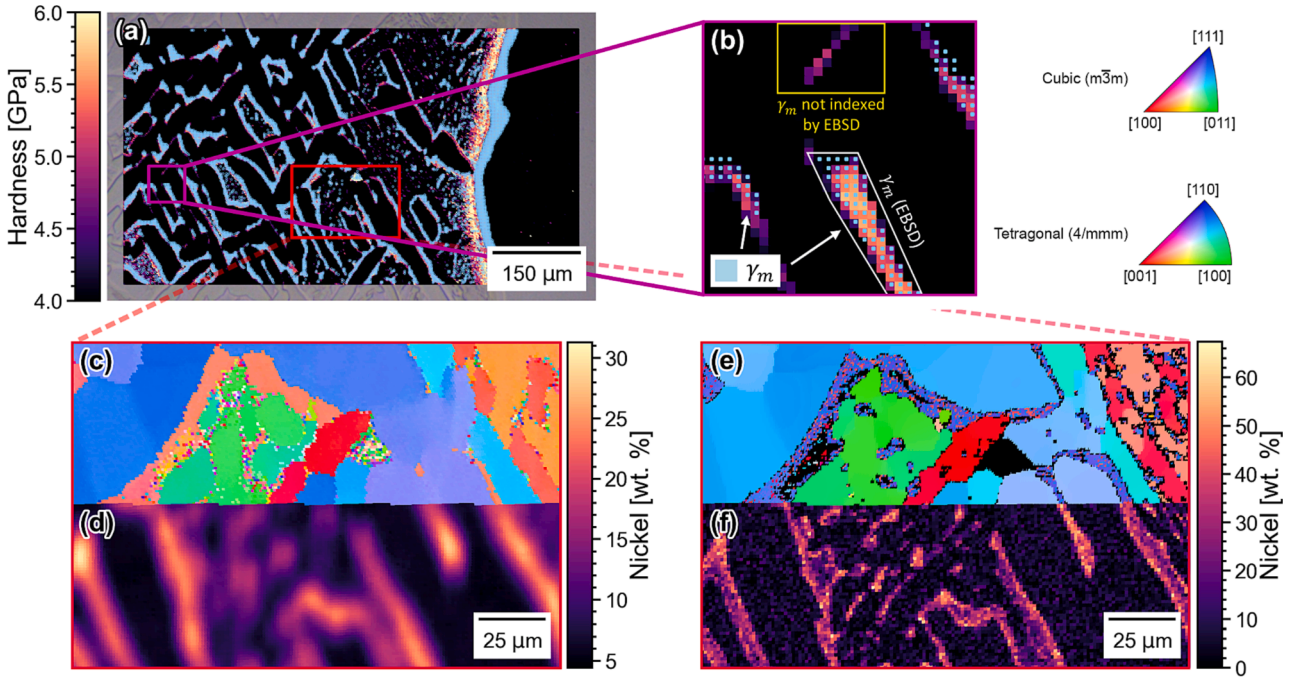


Fig. 17. (a) Hardness plot of the meteorite sample, superimposed with an indentation pattern coloured according to the γ_m phase; (b) indentation map overlayed with correlated EBSD spots revealing a thin γ_m band not indexed by the EBSD measurement highlighted in yellow. The region of this methodological limitation is depicted within the red rectangle. Spatial resolution discrepancy of (c) EBSD and (d) EDS with a detector area window of 60 mm^2. In comparison (e) EBSD (where γ_m is indexed as tetrataenite) with correlated (f) higher precision EDS detected with two large area window detectors of 100 mm^2 after indentation that allowed quantification without binning.

the general speed of the measurement, the sampling rate or due to the high strain rate and closer spacing between the indents [17,55,56]. Consequently, potential sources of error include alignment, interpolation and methodological limitations, whereby alignment could be critical for multi-phase materials if the grain size distribution of the given sample is multi-modal or the aspect ratio of the grains is high. The degree of misalignment was quantified to demonstrate the alignment problems by calculating the proportion of a well aligned rectangular area. Therefore, two surfaces of different sizes but with the same shape are used for demonstration. Exemplary geometries for this calculation are given in Fig. 16 and the corresponding equation is presented in Eq. (16).

Here, l_x and l_y are the lengths of the statistically homogeneous rectangular area along the x- and y-directions, respectively. R_a represents the aspect ratio of the rectangular area, where $\Delta\, l_y$ and $\Delta\, l_x$ denote the displacement of the geometry along the x- and y-directions, respectively.

Assuming that the misalignment in x- and y- direction is equal ($\Delta l_x = \Delta l_y$), the proportion of the correctly aligned surface can be calculated by Eq. (16).

$$\frac{A_{aligned}}{A_{total}} = \frac{\max(0,\ l_x - |\Delta l_x|) \bullet \max(0,\ R_a l_x - |\Delta l_y|)}{R_a {l_x}^2} \tag{16}$$

For a given misalignment Δl in either direction, the well-aligned area scales with the absolute difference between the area's length l and the misalignment. This implies in particular, that the accurately aligned area of the phase with smaller grains or domains tends to decrease faster than that of the phase with larger grains or domains, as shown in Fig. 16b). In addition, the higher the aspect ratio, the faster the well-aligned area decreases for isotropic misalignment. For this reason,

microstructures with a multi-modal grain size distribution or high aspect ratios are challenging to correlate.

Methodological differences also need to be considered. Using the correlated EBSD and nano-indentation data of the meteorite in Fig. 17 as an example, it becomes apparent that a perfect correlation was not feasible, especially within the region containing thin γ_m seams, as some were partially not indexed by EBSD.

Additionally, the incompatibility of different spatial resolutions affects the correlation and needs to be considered. For example, the quantified e-ZAF EDS data of the Seymchan meteorite exhibited a relatively high degree of blur compared to the EBSD data due to binning for better e-ZAF quantification, as shown in Fig. 17c) and d). However, this can be effectively corrected by using improved equipment or acquisition parameters, as shown in Fig. 17e) and f). In addition, it could be that the correlation is less accurate when the point-to-point correlation is performed for fine structures or grain boundary regions. It is also necessary to take into account the intrinsic spatial resolution limitation of the elemental analysis due to the larger interaction volume of the characteristic X-ray emission compared to the backscattered electron emission.

In conclusion, the point-to-point correlation should ideally be performed either between data with similar spatial resolution or with appropriate data filtering methods to avoid erroneous correlations. In general, the observations and results of the two materials investigated in this study were analysed mainly to demonstrate the potential of the newly developed library rather than for scientifically accurate extraction of unknown elastic constants.

Despite the limitations encountered with respect to the fine, two-phase and textured meteorite microstructure, the combinatorial approach of the nano-indentation and the EBSD measurement can provide valuable insights. It was demonstrated that the high-speed NIT can elucidate the single crystal stiffness tensor without the need to solve the complex constitutive equations of the V-N model. As a result of the statistical advantage of high-speed NIT, a reliable estimation of the indentation moduli of low-index planes was possible. Therefore, this study presents further possibilities, such as the use of pre-compiled equation databases for other crystal systems, even if the numerical solutions for other crystallographic systems are not yet fully established.

5. Conclusions

Using a specifically developed point-to-point correlation method between nanoindentation, EBSD and EDS, it was demonstrated that the elastic stiffness tensor can be extracted from indentation data with good agreement between measurement and estimation. For this, we used two different materials, a single phase polycrystal with weak texture and a two-phase material with a strong texture as well as small features compared with the spatial resolution of the correlated measurements. This highlighted both the potential and the limitations of the approach, which are summarised as follows:

1. Using the correlation between the EBSD measurements and high-speed NIT experiments on a single phase austenitic steel demonstrated that the orientation-dependent indentation moduli could be fitted successfully using DFT data for pure iron as starting values.
2. In a second step, this enabled the estimation of the single crystal stiffness tensor based on the pre-solved equation parameters of the V-N model that showed good correspondence with other experimentally obtained single crystal stiffness tensor estimates.
3. Importantly, this analysis is possible without computationally expensive solving of constitutive equations underlying the V-N model.
4. In multi-phase materials with complex microstructures, difficulties are encountered, particularly where the uncertainty in alignment approaches the spatial resolution of the least accurate correlated measurement. However, appropriate filtering allows the extraction of correlated data from suitable regions of interest even if embedded in a microstructure that is ill-suited for correlative analysis as a whole.

Overall, the presented method therefore demonstrates great potential to derive more directionally sensitive elastic properties from indentation with relative ease in the future.

Declaration of Competing Interest

The authors declare that they have no known competing financial interests or personal relationships that could have appeared to influence the work reported in this paper.

Data availability

Data will be made available on request.

Acknowledgement

The authors gratefully acknowledge the Deutsche Forschungsgemeinschaft (DFG, German Research Foundation) for funding their project 406912286 (C-TRAM). This project has also received funding from the European Research Council (ERC) under the European Union's Horizon 2020 Research and Innovation Programme (Grant Agreement No. 852096 FunBlocks). The authors also thank the Scientific Center for Optical and Electron Microscopy (ScopeM), ETH Zurich, for access to its facilities. Additionally, the authors express their gratitude to Prof. Jörg F. Löffler and Dr. Indranil Basu for his assistance with the HR-EDS.

References

[1] J. Gong, A.J. Wilkinson, A microcantilever investigation of size effect, solid-solution strengthening and second-phase strengthening for< a> prism slip in alpha-Ti, Acta Mater. 59 (15) (2011) 5970–5981.
[2] W.C. Oliver, G.M. Pharr, Nanoindentation in materials research: Past, present, and future, MRS Bull. 35 (11) (2010) 897–907.
[3] Y.M. Arısoy, L.E. Criales, T. Özel, B. Lane, S. Moylan, A. Donmez, Influence of scan strategy and process parameters on microstructure and its optimization in additively manufactured nickel alloy 625 via laser powder bed fusion, Int. J. Adv. Manuf. Technol. 90 (5-8) (2017) 1393–1417.
[4] Britton, T., et al., *The effect of crystal orientation on the indentation response of commercially pure titanium: experiments and simulations.* Proceedings of the Royal Society A: Mathematical, Physical and Engineering Sciences, 2010. **466**(2115): p. 695-719.
[5] S. Das, F. Hofmann, E. Tarleton, Consistent determination of geometrically necessary dislocation density from simulations and experiments, Int. J. Plast 109 (2018) 18–42.
[6] M. Quaresimin, Modelling the fatigue behaviour of bonded joints in composite materials, in: Multi-scale Modelling of Composite Material Systems, Elsevier, 2005, pp. 469–494.
[7] H.N. Southworth, Scanning electron microscopy and microanalysis, in: A.W. Nicol (Ed.), Physicochemical Methods of Mineral Analysis, Springer US, Boston, MA, 1975, pp. 421–450.
[8] S.C. Schwarm, R.P. Kolli, E. Aydogan, S. Mburu, S. Ankem, Characterization of phase properties and deformation in ferritic-austenitic duplex stainless steels by nanoindentation and finite element method, Mater. Sci. Eng. A 680 (2017) 359–367.
[9] P. Tao, J.-M. Gong, Y.-F. Wang, Y. Jiang, Y. Li, W.-W. Cen, Characterization on stress-strain behavior of ferrite and austenite in a 2205 duplex stainless steel based on nanoindentation and finite element method, Results Phys. 11 (2018) 377–384.
[10] R. Li, et al., Anisotropy in the elasticity of α-U from first-principles calculations and nanoindentation, J. Nucl. Mater. 558 (2022), 153351.
[11] J.M. Wheeler, Mechanical phase mapping of the Taza meteorite using correlated high-speed nanoindentation and EDX, J. Mater. Res. 36 (1) (2021) 94–104.
[12] J.M. Wheeler, B. Gan, R. Spolenak, Combinatorial investigation of the Ni–Ta system via correlated high-speed nanoindentation and EDX mapping, Small Methods 6 (2) (2022), 2101084.
[13] M. Mejri, et al., Investigation of the mechanical properties of Mn15Si26 via EBSD-nanoindentation coupling and ab-initio calculation, J. Alloy. Compd. 900 (2022), 163458.
[14] C. Fizanne-Michel, M. Cornen, P. Castany, I. Péron, T. Gloriant, Determination of hardness and elastic modulus inverse pole figures of a polycrystalline commercially pure titanium by coupling nanoindentation and EBSD techniques, Mater. Sci. Eng. A 613 (2014) 159–162.

[15] J. Aspinall, D.E.J. Armstrong, M. Pasta, EBSD-coupled indentation: nanoscale mechanics of lithium metal, Mater. Today Energy 30 (2022), 101183.
[16] G. Nolze, Image distortions in SEM and their influences on EBSD measurements, Ultramicroscopy 107 (2–3) (2007) 172–183.
[17] C.M. Magazzeni, H.M. Gardner, I. Howe, P. Gopon, J.C. Waite, D. Rugg, D.E. J. Armstrong, A.J. Wilkinson, Nanoindentation in multi-modal map combinations: a correlative approach to local mechanical property assessment, J. Mater. Res. 36 (11) (2021) 2235–2250.
[18] J. Everaerts, C. Papadaki, W. Li, A.M. Korsunsky, Evaluation of single crystal elastic stiffness coefficients of a nickel-based superalloy by electron backscatter diffraction and nanoindentation, J. Mech. Phys. Solids 131 (2019) 303–312.
[19] J.J. Vlassak, W.D. Nix, Measuring the elastic properties of anisotropic materials by means of indentation experiments, J. Mech. Phys. Solids 42 (8) (1994) 1223–1245.
[20] F. Bachmann, R. Hielscher, H. Schaeben, Texture analysis with MTEX – Free and open source software toolbox, Solid State Phenom. 160 (2010) 63–68.
[21] L. Zou, Q. Zhou, Quantitative analysis of carbon in carbon steel using SEM/EDS followed by error correction approach, Microsc. Microanal. 19 (S2) (2013) 1048–1049.
[22] D. Van Niekerk, et al., Seymchan: a main group pallasite-not an iron meteorite, Meteorit. Planet. Sci. Suppl. 42 (2007) 5196.
[23] M.F. Doerner, W.D. Nix, A method for interpreting the data from depth-sensing indentation instruments, J. Mater. Res. 1 (4) (1986) 601–609.
[24] I.N. Sneddon, The relation between load and penetration in the axisymmetric Boussinesq problem for a punch of arbitrary profile, Int. J. Eng. Sci. 3 (1) (1965) 47–57.
[25] H. Gao, T.-W. Wu, A note on the elastic contact stiffness of a layered medium, J. Mater. Res. 8 (12) (1993) 3229–3232.
[26] C.-M. Cheng (Zheng Zhemin) Institute of Mechanics, Chinese Academy of Sciences, Beijing 100 080, People's Republic of China Y.-T. Cheng Physics and Physical Chemistry Department, General Motors Research and Development Center, Warren, Michigan 48090 On the initial unloading slope in indentation of elastic-plastic solids by an indenter with an axisymmetric smooth profile Applied physics letters 71 18 1997 1997 2623 2625.
[27] S. Marschner, et al., Fundamentals of computer graphics. (2018) 183–231.
[28] Ånes, H.W., et al., *pyxem/orix: orix 0.11.1*. Zenodo.
[29] Pedregosa, F., et al., *Scikit-learn: Machine learning in Python.* Journal of machine learning research. **12**(Oct): p. 2825-2830.
[30] Virtanen, P., et al., *SciPy 1.0: Fundamental algorithms for scientific computing in Python.* Nature Methods. **17**: p. 261-272.
[31] O. Kapikranian, et al., Point defect absorption by grain boundaries in alpha-iron by atomic density function modeling, Phys. Rev. B 92 (22) (2015), 224106.
[32] C. Zener, Ring diffusion in metals, Acta Crystallogr. 3 (5) (1950) 346–354.
[33] R. Hill, The Elastic Behaviour of a Crystalline Aggregate, Proc. Phys. Soc. A 65 (5) (1952) 349–354.
[34] W. Voigt, Lehrbuch der Kristallphysik (Textbook of crystal physics), BG Teubner, Leipzig und Berlin, 1928.
[35] A. Reus, Berechnung der Fliessgrenze von Mischkristallen auf Grund der Plastizitätsbedingungen für Einkristall, Z. Angew. Math. Mech. 9 (1929) 49–58.
[36] M. Laurent-Brocq, E. Béjanin, Y. Champion, Influence of roughness and tilt on nanoindentation measurements: A quantitative model, Scanning 37 (5) (2015) 350–360.
[37] H.M. Ledbetter Cryogenics Division, Institute for Basic Standards, National Bureau of Standards, Boulder, Colorado 80302 R.P. Reed Cryogenics Division, Institute for Basic Standards, National Bureau of Standards, Boulder, Colorado 80302 Elastic properties of metals and alloys, I. Iron, Nickel, and Iron-Nickel alloys Journal of Physical and Chemical Reference Data 2 3 1973 1973 531 618.
[38] G. Alers, J. Neighbours, H. Sato, Temperature dependent magnetic contributions to the high field elastic constants of nickel and an Fe-Ni alloy, J. Phys. Chem. Solid 13 (1–2) (1960) 40–55.
[39] D. Bower, E. Claridge, I. Tsong, Low-temperature elastic constants and specific heats of fcc nickel–iron alloys, physica status solidi (b) 29 (2) (1968) 617–625.
[40] D.E. Diesburg, The elastic constants of iron-nickel-carbon alloys, Iowa State University, 1971.
[41] N.G. Einspruch Texas Instruments Incorporated, Dallas, Texas L.T. Claiborne Texas Instruments Incorporated, Dallas, Texas Elastic Constants of a (73.8% Ni-26.2% Fe) Ferromagnetic Alloy Journal of Applied Physics 35 1 1964 1964 175 175.
[42] E. Goens, E. Schmid, Über die elastische Anisotropie des Eisens, Naturwissenschaften 19 (23–25) (1931) 520–524.
[43] M.W. Guinan, D.N. Beshers, Pressure derivatives of the elastic constants of α-iron to 10 kbs, J. Phys. Chem. Solid 29 (3) (1968) 541–549.
[44] R. Kimura, K. Ohno, On the elastic constants of single crystals of iron, Sci. Rept. Tohoku Univ. (1934) 359–364.
[45] Kimura, R.i., *On the elastic moduli of ferromagnetic materials. Part I. Dynamical measurements of the elastic moduli of iron crystals.* Nippon Sugaku-Buturigakkwai Kizi Dai 3 Ki, 1939. **21**(8-11): p. 686-706.
[46] J. Leese Metals Research Laboratory, Brown University, Providence, Rhode Island A.E. Lord Metals Research Laboratory, Brown University, Providence, Rhode Island Elastic stiffness coefficients of single-crystal iron from room temperature to 500° C Journal of Applied Physics 39 8 1968 1968 3986 3988.
[47] M.F. Markham, Measurement of elastic constants by the ultrasonic pulse method, Br. J. Appl. Phys. 8 (S6) (1957) S56–S63.
[48] J.A. Rayne, B.S. Chandrasekhar, Elastic constants of iron from 4.2 to 300 K, Phys. Rev. 122 (6) (1961) 1714–1716.
[49] C. Rotter, C.S. Smith, Ultrasonic equation of state of iron: I. low pressure, room temperature, J. Phys. Chem. Solid 27 (2) (1966) 267–276.
[50] K. Salama, G. Alers, Elastic moduli variations at the martensitic transformation of a Fe–Ni alloy, J. Appl. Phys. 39 (10) (1968) 4857–4859.
[51] Y. Shirakawa, et al., Elastic constants of Ni and Ni-Fe–fcc– alloys, J Japan Inst. Metals 33 (10) (1969) 1196–1202.
[52] M. Yamamoto, On the elastic constants of iron single crystals, J. Jpn. Inst. Met. 7 (1943) 346–348.
[53] K. Sangwal, Etching of crystals: theory, experiment and application, Elsevier, 2012.
[54] M. Wittwer, M. Seita, A machine learning approach to map crystal orientation by optical microscopy, npj Comput. Mater. 8 (1) (2022) 8.
[55] E.D. Hintsala, U. Hangen, D.D. Stauffer, High-throughput nanoindentation for statistical and spatial property determination, JOM 70 (4) (2018) 494–503.
[56] C.-H. Yu, K.-P. Lin, C.-S. Chen, Nanoindentation and indentation size effects: Continuum model and atomistic simulation, in: S. Schmauder, C.-S. Chen, K. K. Chawla, N. Chawla, W. Chen, Y. Kagawa (Eds.), Handbook of Mechanics of Materials, Springer Singapore, Singapore, 2019, pp. 759–794.
[57] S. Lee, M. Seehaus, PyXC, 2023, Available online: https://zenodo.org/record/8322342 (accessed on 1. September 2023).